Fatigue Crack Growth on Several Materials under Single-Spike Overloads and Aircraft Spectra during Constraint-Loss Behavior

Journal:	*Materials Performance and Characterization*
Manuscript ID	MPC-2023-0074.R1
Manuscript Type:	Technical Manuscript
Date Submitted by the Author:	14-Oct-2023
Complete List of Authors:	Newman, James; Mississippi State University, Aerospace Walker, Kevin; QinetiQ, Aircraft Structural Integrity;
Keywords:	Cracks, stress-intensity factor, crack growth, crack closure, plasticity, overloads, underloads, spectra, aluminum, steel
ASTM Committees and Subcommittees:	E08.06 Crack Growth Behavior < E08 Committee on Fatigue and Fracture
Abstract:	The phenomenon of flat-to-slant crack growth has been studied by many in the Fracture Mechanics community. At low stress-intensity factors, a fatigue-crack surface is flat (tensile mode) and the crack-front region is under plane-strain conditions (high constraint). As the crack grows with higher stress-intensity factors, a 45-degree shear lip occurs through the thickness of the sheet or plate. This behavior is the shear mode, which is under low constraint or plane-stress conditions. In 1966, Schijve found that the transition from flat-to-slant crack growth on a 2024-T3 Alclad aluminum alloy over a wide range in stress ratios (R) occurred at a "constant" crack-growth rate. Also, Newman and Hudson showed the same behavior on 7075-T6 and Ti 8Al-1Mo-1V alloys, validating Schijve's observation that crack-growth rate was the key parameter for flat-to-slant crack-growth behavior. The materials considered herein are 2024-T3, 7075-T6 and 9310 steel. Crack-growth behavior during single-spike overloads and simulated aircraft spectrum loading are presented. The FASTRAN crack-closure based life-prediction code was used to correlate the constant-amplitude crack-growth-rate data over a wide range in stress ratios (R = Smin/Smax) and rates from threshold to near fracture, and to calculate or predict the crack-growth behavior on single-spike overload tests. Crack-closure behavior is strongly dependent upon the level of constraint. The main objective was to see if the constraint-loss region (flat-to-slant crack growth) is the primary reason for crack-growth delays after single-spike overloads. Also, crack-growth analyses are presented on tests that were conducted by Wanhill on 2024-T3 Alclad aluminum alloy under the TWIST (standard European) transport wing spectrum. Crack-growth analyses using crack-closure theory without constraint loss was "unable" to predict crack growth under spike overloads or simulated aircraft spectra. However, predicted crack length

	against cycles with constraint-loss behavior compared reasonably well with all tests.

Fatigue Crack Growth on Several Materials under Single-Spike Overloads and Aircraft Spectra during Constraint-Loss Behavior

James C Newman, Jr[1]* and Kevin F Walker[2]

ABSTRACT

The phenomenon of flat-to-slant crack growth has been studied by many in the Fracture Mechanics community. At low stress-intensity factors, a fatigue-crack surface is flat (tensile mode) and the crack-front region is under plane-strain conditions (high constraint). As the crack grows with higher stress-intensity factors, a 45-degree shear lip occurs through the thickness of the sheet or plate. This behavior is the shear mode, which is under low constraint or plane-stress conditions. In 1966, Schijve found that the transition from flat-to-slant crack growth on a 2024-T3 Alclad aluminum alloy over a wide range in stress ratios (R) occurred at a "constant" crack-growth rate. Also, Newman and Hudson showed the same behavior on 7075-T6 and Ti 8Al-1Mo-1V alloys, validating Schijve's observation that crack-growth rate was the key parameter for flat-to-slant crack-growth behavior.

The materials considered herein are 2024-T3, 7075-T6 and 9310 steel. Crack-growth behavior during single-spike overloads and simulated aircraft spectrum loading are presented.

[1] Aerospace Engineering, Mississippi State University, Mississippi, 39762, USA; 0000-0002-8402-221X
[2] QinetiQ Ltd., South Melbourne, VIC, 3805, Australia; 0000-0003-0614-6564
*Corresponding author: James C. Newman, Jr., jcn3591@gmail,com

The FASTRAN crack-closure based life-prediction code was used to correlate the constant-amplitude crack-growth-rate data over a wide range in stress ratios ($R = S_{min}/S_{max}$) and rates from threshold to near fracture, and to calculate or predict the crack-growth behavior on single-spike overload tests. Crack-closure behavior is strongly dependent upon the level of constraint. The main objective was to see if the constraint-loss region (flat-to-slant crack growth) is the primary reason for crack-growth delays after single-spike overloads. Also, crack-growth analyses are presented on tests that were conducted by Wanhill on 2024-T3 Alclad aluminum alloy under the TWIST (standard European) transport wing spectrum. Crack-growth analyses using crack-closure theory without constraint loss was "unable" to predict crack growth under spike overloads or simulated aircraft spectra. However, predicted crack length against cycles with constraint-loss behavior compared reasonably well with all tests.

Keywords

Cracks, stress-intensity factor, crack growth, crack closure, plasticity, overloads, underloads, spectra, aluminum, steel

Introduction

Fatigue-crack growth in metallic materials has been studied for the past 70 years. The Comet airplane failure in the mid-1950's was instrumental in starting research programs world-wide by many aircraft companies and universities to understand the controlling factors. The development of the principles of Fracture Mechanics, especially the crack-tip stress-intensity factor (K), has provided aircraft designers with a methodology to predict fatigue lives and fatigue-crack growth lives of complex metallic components. In the mid-1960's, the phenomenon of flat-to slant crack growth, as shown in figure 1, was studied by many in the aircraft industry[1]. At low stress-

intensity factors (SIF), a crack surface is very flat, and the behavior is referred to as the tensile crack-growth mode. In addition, the stress state in the crack-front region is under plane-strain conditions or what is called high constraint. As the crack grows with higher stress-intensity factors, a 45-degree shear lip starts to develop at the intersection of the crack front and the free surfaces. At a certain point, with further crack extension, a complete shear failure occurs through the thickness of the sheet or plate. This behavior is the shear mode, which is under low constraint or plane-stress conditions. However, the slant crack still grows perpendicular to the loading direction. Currently, crack-growth calculations during the flat-to-slant crack-growth transition, such as the FASTRAN crack-closure model, is treated as a two-dimensional crack configuration and does not use mixed-mode stress fields to model the opening and sliding modes of deformation. The effects of crack orientation and stress state are embedded in the ΔK-rate correlation. Two-dimensional models have been very successful, but future mixed-mode modelling may provide more information on the stress state and the constraint-loss regime (CLR).

FIGURE 1 Schematic of flat-to-slant fatigue-crack growth in metallic materials.

In 1966, Schijve[2] found that the transition from flat-to-slant crack-growth behavior in a 2024-T3 Alclad aluminum alloy occurred at a "constant" crack-growth rate, independent of stress ratio ($R = S_{min}/S_{max}$). Others at the ASTM Symposium on Crack Propagation[1] had proposed that ΔK or K_{max} controlled the transitional behavior. Newman[3] in a discussion on the subject provided additional test data from the NASA Langley Research Center by Hudson[4,5] on

7075-T6 and Ti 8Al-1Mo-1V alloys to support Schijve's conclusion that crack-growth rate was the controlling parameter.

In studying fatigue-crack growth behavior in a 2024-T3 bare aluminum alloy, Elber[6] discovered the crack-closure phenomenon, whereby the crack surfaces are partially closed under tensile loading. Cracks only grow when the crack tip is fully open, including conditions of "remote closure" where the crack is open at the tip, but the crack faces are in contact for a portion of the crack face behind the tip. He proposed that the effective stress-intensity factor, ΔK_{eff}, controlled the fatigue-crack-growth rates as

$$\Delta K_{eff} = (S_{max} - S_o) \sqrt{(\pi\ c)}\ F \quad (1)$$

where S_{max} is the maximum remote applied stress, S_o is the crack-opening stress, c is crack half-length, and F is the boundary-correction factor. The plasticity-induced crack closure (PICC) concept has revolutionized the analyses of crack growth under constant- and variable-amplitude loading. Elber found that by measuring crack opening stress (and therefore effective SIF) during fatigue crack growth rate (FCGR) testing, the individual FCGR against ΔK data at various stress ratios (R), would collapse into nearly unique FCGR against ΔK_{eff} data.

The FASTRAN life-prediction code multiple-linear crack-growth-rate equation is

$$dc/dN = C_{1i}\ (\Delta K_{eff})^{C_{2i}}\ [1 - (\Delta K_o/\Delta K_{eff})^p]/[1 - (K_{max}/K_{Ie})^q] \quad (2)$$

where C_{1i} and C_{2i} are coefficient and exponent for each linear segment (i = 1 to n), respectively. The ΔK_{eff} is effective stress-intensity factor (Eqn. 1), ΔK_o is effective threshold, K_{max} is maximum stress-intensity factor, K_{Ie} is elastic stress-intensity factor at failure (which is, generally, a function of crack length, specimen width, and specimen type), p and q are constants selected to fit test data in either the threshold or fracture regimes, respectively. Herein, no

threshold was modeled and ΔK_o was set equal to zero; thus, p was not needed. Near-threshold behavior was modeled with the multi-linear equation (independent of *R*). Fracture (K_{Ie}) was modeled using the Two-Parameter Fracture Criterion[7] (TPFC: K_F and m).

Plane-Strain to Plane-Stress Fatigue-Crack-Growth Behavior

Since Schijve showed that flat-to-slant crack growth occurred at a constant rate (dc/dN), then Elber's relation would indicate that ΔK_{eff} controls the flat-to-slant (plane-strain to plane-stress) crack-growth region. In 1992, Newman[8] developed a relation to predict the flat-to-slant crack-growth location as

$$(\Delta K_{eff})_T = 0.5\ \sigma_o\ \sqrt{B} \quad (3)$$

where σ_o is the flow stress (average between the yield stress and ultimate tensile strength) and B is sheet or plate thickness. However, the range of the constraint-loss regime (CLR) had to be estimated by a trial-and-error method using spectrum loading tests. The CLR is expressed in terms of a crack-growth rate ($Rate_1$) at the start of constraint loss (α_1) and a crack-growth rate ($Rate_2$) at the end of constraint loss (α_2). Crack-growth rates lower than $Rate_1$ are under high-constraint conditions (like plane strain), while rates greater than $Rate_2$ are under low-constraint conditions (like plane stress). But the single-spike overload and underload tests may be a way to establish the CLR.

The variation of constraint does not have to be associated with the crack-front orientation based on three-dimensional (3D) elastic-plastic finite-element analyses (EPFEA) of a flat crack (see Newman et.al[9]), but crack-front orientation is a clear indication of constraint loss. The 3D EFFEA showed that constraint variation was linearly related to the log of the stress-intensity factor. Thus, the modeling effort in this study is not centered around the premise that crack-front spatial orientation controls constraint. But constraint variation is controlled by the stress state and ΔK_{eff}.

Fatigue-Crack-Growth Rate against ΔK_{eff} Correlations

The FASTRAN crack-closure model[10] was used to develop the ΔK_{eff}-rate relations for three of the materials used in this study, i.e. 2024-T3 sheet (bare), 7075-T6 sheet (bare), and 9310 steel plate. Details are provided in this section. The ΔK_{eff}-rate relation for the fourth material used in this study, 2024-T3 Alclad aluminum alloy, was obtained from Newman[8].

Aluminum Alloy: 2024-T3 Sheet (Bare)

Crack-growth results from Hudson[4], Dubensky[11] and Phillips[12] on middle-crack tension, M(T), specimens made of 2024-T3 aluminum alloy sheet (thickness B = 2.3 mm) were analyzed using the FASTRAN elastic-plastic crack-closure model[10]. The results are shown in figure 2. The figure shows elastic ΔK_{eff} plotted against crack-growth rate. The data collapsed into a narrow band for all stress ratios over a large range in rates from near threshold to fracture. Some large differences occurred at high stress ratios in the high-rate regime. These tests were conducted at extremely high stress levels (0.75 and 0.95 of the yield stress). Even the FASTRAN elastic-plastic analyses were unable to collapse the data along a unique curve in this region. From a

high-cycle fatigue standpoint, however, this discrepancy has very little influence on total life. However, the elastic-plastic fracture criterion (TPFC, see Newman[7]) used in the analysis conducted here (K_F = 267 MPa√m; m = 1) predicted failure very near to the vertical asymptotes of the test data, see the vertical dashed and dotted lines for R = 0.7 and 0.5 (applied stress at 0.75 and 0.95 of the yield stress). Thus, the high-rate test data was obtained from interrupted stable tearing fracture tests under cyclic loadings.

FIGURE 2 Effective stress-intensity factor range against rate for 2024-T3 bare M(T) specimens.

FASTRAN with a constraint factor (α) of 2.0 was found to correlate the rates in terms of ΔK_{eff} for rates less than 1e-04 mm/cycle and α equal to 1.0 was used for rates greater than 2.5e-03 mm/cycle. For intermediate rates, α was varied linearly with the logarithm of crack-growth rate[13,14]. The values of α and rate were selected by trial-and-error and from analyses of crack growth under spectrum loading[8]. For the 2024-T3 alloy sheet, the effective stress-intensity factor at transition, $(\Delta K_{eff})_T$ = 10.2 MPa√m, fell within the constraint-loss regime. FASTRAN is a two-dimensional model, so the constraint factor (α) is used to account for the three-dimensional stress state that develops around stress risers, holes, notches and cracks. An α value of 1.0 corresponds to pure plane stress and 3.0 corresponds to pure plane strain. The value used in FASTRAN is an average value over the crack front and through the thickness. The issue of constraint is very important in determining the extent of the plastic zone ahead of the crack tip and the wake of plastically deformed material remaining in the crack wake. These issues drive the level of closure and, thus, have a very significant effect on the effective stress intensity factor range and crack growth. In the low crack-growth rate regime, near the large-crack threshold,

tests and analyses have shown that thresholds develop because of a rise in the crack-opening stresses due to the load-shedding procedure (see Newman[15]). In the threshold regime, the actual ΔK_{eff} -rate data would lie at lower values of ΔK_{eff} because the rise in crack-opening stress was not accounted for in the current analysis. For the present study, an estimate was made for this behavior using small-crack data (see Newman and Edwards[16]) and it is shown by the solid line below rates of about 2e-06 mm/cycle. The vertical dashed line in the small-crack regime shows an estimate for the effective stress-intensity-factor threshold, $(\Delta K_{eff})_{th}$, based on the modulus of elasticity[17].

The ΔK_{eff} -rate curve (solid lines with circular symbols) was obtained by manually selecting the points to fit the data. In the small-crack regime, the curve was estimated on the basis of small-crack data and the estimated threshold based on the modulus of elasticity. See Table 1 for the effective stress-intensity factor range against rate, fracture and tensile properties for 2024-T3 bare sheet (B = 2.3 mm).

Table 1. Effective stress-intensity factor range against rate, fracture, and tensile properties for 2024-T3 bare sheet (B = 2.3 mm).

ΔK_{eff} (MPa-m$^{1/2}$)	dc/dN (m/cycle)	Crack-growth, fracture and tensile properties	
0.80	2.0e-12	$\Delta K_o = 0$	q = 0
1.05	1.0e-10	$\alpha_1 = 2.0$	1.0e-7 m/cycle
1.35	6.0e-10	$\alpha_2 = 1.0$	2.5e-6 m/cycle
1.80	2.0e-9	K_F =	267 MPa-m$^{1/2}$
4.00	8.0e-9	m =	1.0
7.30	1.0e-7	σ_{ys} =	356 MPa
14.0	1.0e-6	σ_u =	490 MPa
23.5	1.0e-5	σ_o =	423 MPa

37.0	1.0e-4	E =	71.7 GPa
85.0	1.0e-2	---	---

Aluminum Alloy: 7075-T6 Sheet (Bare)

Herein, the results of fatigue-crack-growth tests made on M(T) specimens are compared with previous test data from the NASA Langley Research Center on the same material[4,18] in the constraint-loss region (CLR). The current tests at R = 0 loading were designed to propagate a crack across the CLR. Crack length and crack-opening loads were measured from the crack-monitoring system[19] using crack-mouth-opening-displacement (CMOD) gauges. The zero-percent compliance offset value was determined from the 1 and 2% offset values[20] as OP0 = 2 OP1 – OP2. (OPn is the compliance offset value at n-percent[20].)

Figure 3 shows ΔK against crack-growth rate (dc/dN) for R = 0 loading. The new test data (solid symbols) compared well over more than 2-orders of magnitude in rates. The two horizontal lines show the start and end of the estimated CLR that was determined many years ago by trial-and-error procedures. The light grey symbols are ΔK_{eff} data determined using Equation 1 from a crack-monitoring system[19] which applies the ASTM offset compliance method[20], using the zero-percent compliance offset values determined from the measured 1- and 2-precent offset values to determine the crack-opening stress So . The measured ΔK_{eff}-rate data agreed well with the ΔK_{eff} curve (lines with circular symbols) established many years ago for rates larger than 10^{-4} mm/cycle. See Table 2 for the effective stress-intensity factor range against rate, fracture and tensile properties for 7075-T6 bare sheet (B = 2.3 mm).

FIGURE 3 Stress-intensity-factor range against rate for 7075-T6 bare M(T) specimens.

Table 2. Effective stress-intensity factor range against rate, fracture, and tensile properties for 7075-T6 bare sheet (B = 2.3 mm).

ΔK_{eff} (MPa-m$^{1/2}$)	dc/dN (m/cycle)	Crack-growth, fracture and tensile properties	
0.90	1.0e-11	$\Delta K_o = 0$	q = 6
1.25	1.5e-10	$\alpha_1 = 1.8$	7.0e-7 m/cycle
3.40	4.0e-10	$\alpha_2 = 1.2$	7.0e-6 m/cycle
5.20	1.0e-9	K_F =	124 MPa-m$^{1/2}$
11.9	2.0e-9	m =	0.85
20.0	1.0e-8	σ_{ys} =	520 MPa
50.0	1.0e-7	σ_u =	570 MPa
88.0	8.0e-7	σ_o =	545 MPa
---	---	E =	71.7 GPa

Figure 4 shows P_o/P_{max} plotted against c/w for the two low-R tests. The horizontal dashed lines show the crack-opening-load ratio for plane-strain (α = 3) and plane-stress (α = 1) behavior. Tests B1 and B5 were tested at S_{max} = 50 MPa and R = 0.1 at 0.5 hz, which showed a rise in the crack-opening ratio for c/w > 0.5. The very low frequency was used to reduce the mechanical noise from the CMOD gauges to improve crack-opening load measurements. Measurements of P_o/P_{max} from the experiments showed large scatter but showed the correct trend. The curve was calculated crack-opening-load ratios from FASTRAN[14] using the current constraint-loss regime (see fig. 3).

FIGURE 4 Crack-opening-load ratio as a function of crack-length-to-width ratio for 7075-T6 sheet M(T) specimens.

Steel: 9310 Plate

Compact, C(T), specimens were used to generate the ΔK against rate (dc/dN) data[21,22] on the 9310 steel at room temperature and 20 Hertz over a wide range in stress ratios (R = 0.1 to 0.95). Tests were conducted from near threshold to fracture. A back-face strain (BFS) gauge was used to monitor crack growth and to measure crack-opening loads using the compliance-offset method. In the low-rate regime, compression pre-cracking constant amplitude (CPCA) and load reduction (CPLR) methods were used to generate ΔK-rate data[23,24] to minimize load-history effects from the load-shedding method[20].

A crack-closure analysis was performed on the fatigue-crack growth (ΔK-rate) data from the C(T) specimens to determine the ΔK_{eff}-rate relation. The K-analogy concept[13,14] as described here was used to calculate the crack-opening stresses (or loads) for C(T) specimens. The crack-opening stress equations in FASTRAN were developed for a through crack in a large-width middle-crack tension specimen subjected to remote applied stress. It is impractical to develop these equations for all crack configurations. Because the compact specimen is used quite often to obtain laboratory crack-growth rate data, crack-opening stress expressions are needed to develop baseline ΔK_{eff}-rate relations. A simple approximation can be made to estimate crack-opening stresses. The approximation is based on matching stress intensity factors from the compact specimen to that for a middle-crack tension specimen. A stress S'max is applied to a middle-crack specimen having the same crack length and width as the configuration of interest so that the same stress-intensity factor is developed. Thus, the plastic-zone size (under small-scale yielding), the local crack surface displacements, the local residual plastic deformations and the crack-opening stresses would be nearly the same in both configurations. This approach is called "K-analogy". Note that the K-analogy concept was not required for the other materials (2024-T3 and 7075-T6) because the tests in those cases used middle-crack tension, M(T), specimens – a

configuration for which the FASTRAN crack-opening stress equations were explicitly developed. The ΔK_{eff}-rate data are shown in figure 5.

FIGURE 5 Effective stress-intensity factor range against rate for 9310 steel C(T) specimens.

Selection of the lower constraint factor, $\alpha = 2.5$, was found to reasonably collapse the ΔK-rate data onto an almost unique relation. In the threshold region, the lower R tests exhibited a rise in crack-opening loads as the ΔK level was reduced in a load-reduction test. Even the CPLR test method showed a load-history effect, but not as much as the current ASTM procedure[20]. The upper constraint factor, 1.15, and constraint-loss range was selected to help fit spectrum crack-growth tests[24]. The lower vertical dashed line at $(\Delta K_{eff})_{th}$ is the estimated threshold for the steel[17]; and the upper vertical dashed line at $(\Delta K_{eff})_T$ is the location of constraint loss from plane-strain to plane-stress behavior[8]. The solid lines with circular symbols shows the baseline crack-growth-rate curve for FASTRAN. See Table 3 for the effective stress-intensity factor range against rate, fracture and tensile properties for 9310 steel (B = 6.35 mm).

Table 3. Effective stress-intensity factor range against rate, fracture, and tensile properties for 9310 steel (B = 6.35 mm).

ΔK_{eff} (MPa-m$^{1/2}$)	dc/dN (m/cycle)	Crack-growth, fracture and tensile properties	
2.30	1.0e-11	$\Delta K_o = 0$	q = 6
2.45	1.5e-10	$\alpha_1 = 2.5$	1.0e-7 m/cycle
2.80	4.0e-10	$\alpha_2 = 1.15$	1.0e-5 m/cycle
3.50	1.0e-9	K_F =	500 MPa-m$^{1/2}$
4.40	2.0e-9	m =	0.5
9.50	1.0e-8	σ_{ys} =	980 MPa

20.0	1.0e-7	σ_u =	1,250 MPa
50.0	8.0e-7	σ_o =	1,115 MPa
120.0	6.0e-6	E =	208.6 GPa

The test data at high rates shown in figure 5 illustrates an issue with the test-specimen width. Small width specimens may fracture during or before the CLR, which makes it difficult to establish the region. Large width specimens were used to generate the test data shown in figure 2 and the CLR was transitioned in a stable manner before fracture. Small test specimens are satisfactory for low rates near threshold, but large width specimens are needed to generate test data at high rates and fracture toughness.

Single-Spike Overload/Underload Tests and Analyses

The loading sequence that was applied during single-spike overload/underload testing is shown in figure 6. A crack was grown from the crack-starter notch under constant-amplitude (CA) loading at a given maximum load level and R for N_{CA} cycles. A single-spike overload at OL value was statically applied, and then an underload at UL value was applied. CA loading was then continued until steady-state behavior was achieved. Then another OL and UL was applied, and the crack grown under CA loading to a specified crack length. The specimen was then statically pulled to failure to determine the fracture toughness.

FIGURE 6 Single-spike overload/underload sequence under constant-amplitude loading.

Aluminum Alloy: 2024-T3 Alclad Plate

Yisheng and Schijve[25] conducted single-spike overload and underload tests on M(T) specimens made of 6.35 mm-thick aluminum alloy. See Table 4 for the effective stress-intensity factor

range against rate, fracture and tensile properties for the 2024-T3 Alclad plate. In one specimen, a crack was grown from an initial size to c = 3 mm at S_{max} = 100 MPa and R = 0 constant-amplitude (CA) loading. At this point, a 200 MPa overload (S_{OL}) was applied and the test was continued at the previous constant-amplitude loading. During these tests, the crack-length-against-cycles and crack-opening stresses were measured during and after the overload. Measured and predicted crack-length-against-cycles from the test is shown in figure 7. Note that the predicted cycles have been shifted to match crack length and cycles at the initial crack length (solid symbol). The solid (black) curve shows crack-growth predictions made in 1997 using FASTRAN Version 3.0, which used block loading (NMAX = 300) to speed-up calculations[26]. Recently, FASTRAN Version 5.76 (cycle-by-cycle calculations) was used to make the same predictions and the results are shown as the solid (blue) curve, which agreed better with the test data. The same CLR was used in both predictions. To illustrate the influence of the CLR, a prediction was made using "constant" constraint (α = 2) and these results are shown as the dashed (blue) curve, which showed very little influence of the overload. Thus, using the CLR, the spike overload activated plane-stress behavior that caused an overload plastic-zone size nearly 7.4 times larger than constant constraint and caused much more crack-growth delay due to higher crack-opening loads.

Table 4. Effective stress-intensity factor range against rate, fracture, and tensile properties for 2024-T3 Alclad Plate (B = 6.35 mm).

ΔK_{eff} (MPa-$m^{1/2}$)	dc/dN (m/cycle)	Crack-growth, fracture and tensile properties	
1.0	3.90e-10	ΔK_o = 0	q = 0
2.0	4.41e-9	α_1 = 2.0	1.0e-7 m/cycle
5.0	1.09e-7	α_2 = 1.2	7.0e-6 m/cycle

10.0	1.23e-6	K_F =	267 MPa-$m^{1/2}$
20.0	1.40e-5	m =	1.0
50.0	3.45e-4	σ_{ys} =	360 MPa
100.0	3.90e-3	σ_u =	490 MPa
---	---	σ_o =	425 MPa
---	---	E =	72 GPa

FIGURE 7 Measured and predicted crack-length-against-cycles under a single-spike overload.

The measured crack length against cycles from another Yisheng-Schijve test with an underload, following the same overload as used in figure 7, is shown in figure 8. These results show that the overload causes an almost immediate crack-growth delay and that the application of the underload, immediately after the overload, reduced some of the crack-growth delay caused by the overload (see the delay in figure 7). The solid curves show the predicted results using FASTRAN Version 3.0 or 5.76. Again, the solid symbol shows where the analyses had been anchored. The analyses are in reasonable agreement with the test data. The latest version prediction was closer to the test data than the older version. But the shape of the predicted curve was not exactly the same as the test data. During an overload, a crack will grow more in the interior than at the free surface and during fatigue cracking at the lower stress level, the crack front will grow faster at the free surface than in the interior because of the elevated K level at the free surfaces. The model, on the other hand, is averaging the behavior through the thickness. The closure model accurately predicted the reduction in crack-growth delay due to the compressive underload.

FIGURE 8 Measured and predicted crack-length-against-cycles under a single-spike overload followed by an underload.

A comparison of measured and predicted crack-opening stresses for the single-spike overload and overload-underload tests are shown in figures 9 and 10, respectively. The predicted results using both FASTRAN versions agreed reasonably well with the measured trends. The model tended to predict slightly lower values during the constant-amplitude portion but predicted slightly higher crack-opening stresses after the overload. The length of influence of the overload in terms of cycles, however, was predicted well by both models. These test results and analyses occurred almost exclusively in the CLR (α varied from 2 to 1.2). The saw-tooth nature of the predicted results from Version 3.0 was due to the lumping procedure used to eliminate elements in the model to maintain model efficiency and speed. This saw-tooth behavior was not observed in the cycle-by-cycle version. The difference between the predicted crack-opening stresses (solid curve) and the upper dashed line (S_{max}) gives the effective stress range that is used to compute the effective stress-intensity factor range and, thus, the crack-growth rate.

FIGURE 9 Measured and predicted crack-opening stress under a single-spike overload.

FIGURE 10 Measured and predicted crack-opening stress under a single-spike overload followed by an underload.

Aluminum Alloy: 2024-T3 Sheet (Bare)

For the 305-mm wide thin-sheet 2024-T3 alloy, the end of the estimated CLR is well below the crack-growth rate at fracture, see figure 2. However, in the current study, smaller width M(T)

specimens were used to study the CLR. Thus, fracture tests were needed to accurately predict failure, so that crack-growth tests could be used to generate test data at high rates. Anti-buckling guide plates were used in the fracture tests to help prevent buckling. The elastic stress-intensity factor at fracture, K_{Ie}, is plotted against c_i/w ratio in figure 11. Circular symbols are test data from Newman[28] on larger width specimens and square symbols are tests conducted on 96.5-mm width M(T) specimens. The larger width specimens failed at larger values of K_{Ie} than the smaller width specimens. Solid and dashed curves in figure 9 are the calculated K_{Ie} at failure from the TPFC for net-section stress (S_n) less or greater than the proportional limit of the material (σ_{pl}). For S_n less than σ_{pl}, $K_F = K_{Ie}/(1 - m\ S_n/\sigma_u)$ and for $S_n > \sigma_{pl}$, a more complicated equation was developed[28]. In the TPFC, the fracture toughness parameter m = 0 for linear-elastic fracture mechanics (brittle fracture) and m = 1 for very ductile materials. For the thin-sheet aluminum alloy, the elastic-plastic fracture toughness K_F = 267 MPa-$m^{1/2}$ and m = 1. (Ouidadi[29] using an elastic-plastic finite-element analysis with the critical crack-tip-opening-angle (CTOA) failure criterion on an aluminum alloy validated the TPFC. Her work indicated that the separation between linear and non-linear fracture behavior in the TPFC equations was the proportional limit and not the yield stress of the material.)

FIGURE 11 Measured and calculated elastic fracture toughness for 2024-T3 bare sheet.

The results of a repeated single-spike overload/underload test (solid circular symbols) are shown in figure 12 on a 2024-T3 M(T) specimen. Test A4 was subjected to S_{max} = 55 MPa at R = 0.01 loading and a frequency (f) of 2 hz after 20,000 compression cycles at S_{max} = 0 and S_{min} = - 70 MPa. The crack was initiated at the crack-starter notch (c_n = 9 mm) and grown to c = 14

mm. Here, a factor of 2 overload (110 MPa) was statically applied and then unloaded to zero (UL = 0). CA loading resumed and the crack was grown to 19 mm, where another factor of 2 overload was applied.

FASTRAN Version 5.76 was used to predict crack growth using the ΔK_{eff}-rate curve (see fig. 2) and the CLR that had previously been determined for the thin-sheet alloy[14]. The dashed curve is under CA loading while the solid (blue) curve is under the repeated spike overload/underload test. The model predicted the crack-growth delay from the first and second overloads reasonably well. The dash-dot curve shows the results for constant constraint ($\alpha = 2$), which predicted very little crack-growth delay after both overloads.

FIGURE 12 Measured and predicted crack-length-against-cycles under single-spike overloads on 2024-T3 bare sheet.

Aluminum Alloy: 7075-T6 Sheet (Bare)

Herein, the results of fracture tests conducted on smaller width M(T) specimens are compared with previous tests on wider M(T) specimens from the NASA Langley Research Center on the same material. The elastic stress-intensity factor at fracture, K_{Ie}, is plotted against c_i/w ratio in figure 13. Circular symbols are test data from Hudson[4] on larger width (305-mm) specimens and the square symbols are tests conducted herein on the 96.5-mm width M(T) specimens. The larger width specimens failed at larger values of K_{Ie} than the smaller width specimens. For the thin-sheet aluminum alloy, the elastic-plastic fracture toughness K_F = 124 MPa-$m^{1/2}$ and m = 0.85. Solid and dashed curves are calculated K_{Ie} values at failure from the TPFC for net-section stresses (S_n) less or greater than the proportional limit of the material (σ_{pl}). The larger width

specimens showed more scatter than the smaller width specimens, but 70% of the failure values were within +/- 5% of the solid curve.

FIGURE 13 Measured and calculated elastic fracture toughness for 7075-T6 bare sheet.

The results of a repeated single-spike overload test (solid circular symbols) are shown in figure 14 on a 7075-T6 M(T) specimen. Test B8 was subjected to S_{max} = 75 MPa at R = 0.01 loading and a frequency (f) of 2 hz after 20,000 compression cycles at S_{max} = 0 and S_{min} = - 70 MPa. The crack was initiated at the crack-starter notch (c_n = 5 mm) and grown to c = 10 mm. Here, a factor of 2 overload (150 MPa) was statically applied and then unloaded to zero (UL = 0). CA loading resumed and the crack was grown to 15 mm, where another factor of 2 overload was applied.

Again, FASTRAN Version 5.76 was used to predict crack growth using the ΔK_{eff}-rate curve (see fig. 3) and the CLR that had previously been determined for the thin-sheet alloy[14]. The dashed curve is under CA loading while the solid (blue) curve is under the repeated spike overload/underload test. The model over predicted the delay from the first overload but was reasonable for the second overload. These results suggest that the start of the CLR needs to be moved to a slightly higher rate, so that less delay would occur. The dash-dot curve shows the results for constant constraint (α = 1.8), which predicted very little crack-growth delay after both overloads.

FIGURE 14 Measured and predicted crack-length-against-cycles under single-spike overloads on 7075-T6 bare sheet.

Steel: 9310 Plate

The results of a repeated single-spike overload/underload test (open circular symbols) are shown in figure 15 on a 9310 steel C(T) specimen. The specimen was subjected to $S_{max} = P_{max}/(WB) =$ 10.7 MPa at R = 0.1 loading with a frequency (f) of 18 hz after compression pre-cracking. The crack was initiated at the crack-starter notch and grown to c = 39 mm under CA loading. Here, a factor of 2 overload was statically applied and then unloaded to zero load. CA loading was resumed and the crack was grown to 54 mm, where a factor of 2.5 overload was applied.

FIGURE 15 Measured and predicted crack-length-against-cycles under single-spike overloads on 9310 steel.

FASTRAN Version 5.42 was used to predict crack growth using the ΔK_{eff}-rate curve (see fig. 5) and the CLR that had previously been determined[25]. The dashed curve is under CA loading while the solid (blue) curve is under the repeated spike overload/underload test. Here the overloads were applied on the basis of cycles instead of crack length. The model predicted a slight delay from the first overload and was very reasonable for the second overload. The dashed curve shows the results of constant constraint ($\alpha = 2.5$), which predicted very little crack-growth delay after the overloads.

Aircraft Spectrum Loading Tests and Analyses

As pointed out by Wanhill and Schijve[30], the ability to predict crack-growth behavior under the TWIST[31] spectrum loading has eluded the empirical crack-growth (retardation and acceleration) models in the literature. The exceedance diagram for the TWIST loading is given in Reference

31. However, the strip-yield models, such as those developed by Dill and Saff[32], Fuhring and Seeger[33], Newman[9], and de Koning and Liefting[34] probably have a reasonable chance of predicting such behavior. These models have numerical "memory" to account for the occurrence of overloads, underloads and overlapping plastic zones and should be able to characterize the plastic and residual plastic deformation histories generated under the TWIST spectrum. As will be presented later, the constraint factor plays a leading role in allowing the strip-yield model to predict the crack-opening stress history that develops under the TWIST spectrum. In the following sections, the closure model will be used with the baseline ΔK_{eff}-rate relations, previously determined, to calculate crack growth in a 2024-T3 Alclad aluminum alloy sheet material under a version of the TWIST spectrum.

Wanhill[35,36] conducted spectrum crack-growth tests on M(T) specimens made of 2024-T3 Alclad material in two thicknesses (B = 1.6 and 3.1 mm). Only the results on the thicker material will be shown herein. See Table 5 for the effective stress-intensity factor range against rate, fracture and tensile properties for the 2024-T3 Alclad sheet. Crack-length-against-flight data on the 3.1 mm-thick specimens tested under the TWIST (Level III) loading are shown in figure 16 as open symbols. Level III loading is where all maximum loads higher than Level III are clipped at Level III peak magnitude, such that loads at Level I and II are not applied but the cycle at Level III is applied. Tests were conducted at a mean stress level of S_{mf} = 70 MPa. The initial crack starter notch half-length was 3.5 mm. Comparisons are made between experimental and predicted crack length against flights.

The solid curve is the calculated results from the closure model with the variable-constraint condition (α = 2 to 1) using the baseline ΔK_{eff}-rate relation[7]. Using the CLR established for the aluminum alloy and the model, the predicted results agreed well with the tests (within 15

percent). To illustrate why the variable-constraint conditions are necessary, example calculations are made for constant constraint conditions of either $\alpha = 1$ or 2 (dashed-dot curves). The model with a low constraint condition ($\alpha = 1$) predicted slightly longer flights to a given crack length than the test data for the thin material but predicted much longer lives for the thick material.

Table 5. Effective stress-intensity factor range against rate, fracture, and tensile properties for 2024-T3 alclad sheet (B = 3.1 mm).

ΔK_{eff} (MPa-m$^{1/2}$)	dc/dN (m/cycle)	Crack-growth, fracture and tensile properties	
1.05	1.0e-11	$\Delta K_o = 0$	q = 0
1.05	1.0e-10	$\alpha_1 = 2.0$	1.0e-7 m/cycle
2.20	2.0e-9	$\alpha_2 = 1.0$	3.5e-6 m/cycle
4.10	1.0e-8	K_F =	267 MPa-m$^{1/2}$
7.60	1.0e-7	m =	1.0
10.7	4.0e-7	σ_{ys} =	360 MPa
17.0	3.0e-6	σ_u =	490 MPa
35.0	1.0e-4	σ_o =	425 MPa
---	---	E =	72 GPa

Concluding Remarks

The phenomenon of flat-to-slant crack growth has been associated with plane-strain to plane-stress crack-growth behavior. A structural component with a crack growing under pure plane-

strain (α = 3) conditions (flat crack surfaces) and then subjected to an overload that is large enough to activate constraint loss under plane-stress (α = 1) conditions, the crack front develops a plastic-zone size nearly an order-of-magnitude larger than under plane-strain conditions. The larger plastic-zone size would greatly influence crack-growth behavior and the increased crack-closure behavior would cause much more crack-growth delay.

Schijve's discovery that the transition from flat-to-slant crack growth occurred at a "constant" crack-growth rate and Elber's discovery of plasticity-induced crack closure lead to the development of the transition being expressed in terms of ΔK_{eff}, sheet or plate thickness, and material stress-strain properties.

The materials considered herein are 2024-T3 (Alclad and bare), 7075-T6 (bare) and 9310 steel. Crack growth during single-spike overload behavior and simulated aircraft spectrum loading were presented. The FASTRAN crack-closure based life-prediction code was used to correlate the constant-amplitude crack-growth-rate data over a wide range in stress ratios (R) and rates from threshold to fracture, and to calculate or predict the crack-growth behavior on the single-spike overload tests. Also, crack-growth analyses are presented on tests that were conducted by Wanhill on 2024-T3 Alclad aluminum alloy under the TWIST (standard European) transport wing spectrum. Crack-growth analyses using crack-closure theory without constraint loss were unable to predict crack growth under spike overloads or simulated aircraft spectra. However, predicted crack length against cycles with constraint-loss behavior compared reasonably well with all tests.

FIGURE 16 Measured and predicted crack-length-against-cycles under TWIST spectrum loading.

Acknowledgements

This work was partially supported by Fatigue and Fracture Associates LLC, USA; Mississippi State University, USA and QinetiQ Limited, Australia.

References

1. Fatigue Crack Propagation, ASTM STP 415 (American Society for Testing Materials, Philadelphia, PA., 1967).

2. J. Schijve, "Significance of Fatigue Cracks in Micro-Range and Macro-Range," In: Fatigue Crack Propagation, ASTM STP 415 (American Society for Testing Materials, Philadelphia, PA., 1967), 415-459.

3. J. C. Newman, Jr. "Discussion on Cyclic Crack Growth Transitional Behavior," In: Fatigue Crack Propagation, ASTM STP 415 (American Society for Testing Materials, Philadelphia, PA., 1967), 380-383.

4. C. M. Hudson. "Effect of Stress Ratio on Fatigue-Crack Growth in 7075-T6 and 2024-T3 Aluminum Alloy Specimens," NASA TN D-5390, 1969.

5. C. M. Hudson. "Studies of Fatigue Crack Growth in Alloys Suitable for Elevated Temperature Applications," NASA TN D-2743, 1965.

6. W. Elber. "Fatigue Crack Closure under Cyclic Tension," *Engineering Fracture Mechanics*, 2, no. 1 (1970) 37-45.

7. J. C. Newman, Jr. "Fracture Analysis of Surface- and Through-Cracked Sheets and Plates," Engineering Fracture Mechanics, Vol. 5, No. 3, 1973, pp. 667-689..

8. J. C. Newman, Jr. "Effects of Constraint on Crack Growth under Aircraft Spectrum Loading," In: Fatigue of Aircraft Materials, A. Beukers et al., eds., Delft University Press, 1992, 83-109.

9. J. C. Newman, Jr., C. A. Bigelow and K. N. Shivakumar, "Three-Dimensional Elastic-Plastic Finite-Element Analyses of Constraint Variations in Cracked Bodies," Engineering Fracture Mechanics, Vol. 46, No. 1, 1993, pp. 1-13.

10. J. C. Newman, Jr. "A Crack-Closure Model for Predicting Fatigue Crack Growth Under Aircraft Spectrum Loading," In: Methods and Models for Predicting Fatigue Crack Growth under Random Loading, J. B. Chang and C. M. Hudson, eds., *ASTM STP 748*, 1981, 53-84.

11. R. G. Dubensky. "Fatigue Crack Propagation in 2024-T3 and 7075-T6 Aluminum Alloys at High Stresses," NASA CR-1732, 1971.

12. E. P. Phillips. "The Influence of Crack Closure on Fatigue Crack Thresholds in 2024-T3 Aluminum Alloy," In: Mechanics of Fatigue Crack Closure, J. C. Newman, Jr. and W. Elber, eds., *ASTM STP 982* (American Society for Testing Materials, Philadelphia, PA., 1988) 505-515.

13. J. C. Newman, Jr. "FASTRAN II - Fatigue Crack Growth Structural Analysis Program," NASA TM 104159, 1992.

14. J. C. Newman, Jr. "FASTRAN—A Fatigue Crack Growth Life Prediction Code Based on the Crack-Closure Concept," Version 5.4 User Guide, Fatigue and Fracture Associates LLC, Eupora, MS, USA, 2013.

15. J. C. Newman, Jr. "A Nonlinear Fracture Mechanics Approach to the Growth of Small Cracks. Behaviour of Short Cracks in Airframe Components," In: Behaviour of Short Cracks in Airframe Components, ed. H. Zocher. AGARD CP-328, 1983, 6.1-6.26.

16. J. C. Newman, Jr. and P. R. Edwards. "Short-Crack Growth Behaviour in an Aluminum Alloy - An AGARD Cooperative Test Programme," AGARD R-732, 1988.

17. J. C. Newman, Jr., K. Kota and T. E. Lacy. "Fatigue and Crack-Growth Behavior in a Titanium Alloy under Constant-Amplitude and Spectrum Loading," *Engineering. Fracture Mechanics*, 187 (2018): 211-224.

18. J. C. Newman, Jr., X. R. Wu, S. L. Venneri and C. G. Li. "Small-Crack Effects in High-Strength Aluminum Alloys - A NASA/CAE Cooperative Program," NASA RP-1309, 1994.

19. J. K. Donald and A. Blair. "Automated Fatigue Crack Growth Testing and Analysis – Series 2001. Ver. 3.09," Fracture Technology Associates, LLC, Bethlehem, PA, 2009.

20. Standard Test Method for Measurement of Fatigue Crack Growth Rates, ASTM E-647 (West Conshohocken, PA: ASTM International, approved 2016).

21. J. C. Newman, Jr., A. Vizzini and Y. Yamada. "Fatigue-Crack-Growth Databases and Analyses for Threshold Behavior in Rotorcraft Materials," Department of Transportation, DOT/FAA/AR-10/3, Washington, D.C., USA, 2010.

22. J. C. Newman, Jr. "Fatigue and Crack Growth under Constant- and Variable- Amplitude Loading in 9310 Steel Using 'Rainflow-On-The-Fly' Methodology," *Metals*, 11 (2021): 807. https://doi.org/10.3390/met11050807.

23. Y. Yamada and J. C. Newman, Jr. "Crack Closure under High Load-Ratio Conditions for Inconel 718 near Threshold Behavior", *Engineering Fracture Mechanics*, 76, (2009): 209-220.

24. Y. Yamada and J. C. Newman, Jr. "Crack Closure Behavior of 2324-T39 Aluminum Alloy near Threshold Conditions for High Load Ratio and Constant K_{max} Tests", *International Journal of Fatigue*, 31 (2009): 1780-1787.

25. J. C. Newman, Jr., Y. Yamada, B. M. Ziegler and J. W. Shaw. "Small and Large Crack Damage Tolerance Database for Rotorcraft Materials," Department of Transportation, DOT/FAA/TC-13/29, Washington, D.C., USA, 2014.

26. Wu Yisheng and J. Schijve. “Fatigue Crack Closure Measurements on 2024-T3 Sheet Specimens,” *Fatigue and Fracture of Engineering Materials and Structures,* 18 (1995): 917-921.

27. J. C. Newman, Jr. “Crack Growth under Variable Amplitude and Spectrum Loading,” In: High Cycle Fatigue of Structural Materials, W. O. Soboyejo and T. S. Srivatsan, eds. (The Minerals, Metals & Materials Society, 1997), 109-121.

28. J. C. Newman, Jr. “Fracture Analysis of Various Cracked Configurations in Sheet and Plate Materials,” In: Properties Related to Fracture Toughness. ASTM STP 605 (American Society for Testing Materials, Philadelphia, PA., 1976) 104-123.

29. H. Ouidadi, H. Validation of the Two-Parameter Fracture Criterion using Critical CTOA on 7075-T6 Aluminum Alloy,” MS Thesis, Mississippi State University, USA, 2017.

30. R. J. H. Wanhill and J. Schijve. “Current Status of Flight Simulation Fatigue Crack Growth Concepts,” NLR MP 88001 U, 1988.

31. J. B. de Jonge, D. Schutz, H. Lowak, H. and Schijve, J. A Standardized Load Sequence for Flight Simulation Tests on Transport Aircraft, LBF-Bericht FB-106 & NLR TR 73029 U, 1973.

32. H. D. Dill and C. R. Saff, “Spectrum Crack Growth Prediction Method Based on Crack Growth Surface Displacement and Contact Aanalysis,” *ASTM STP 595* , (American Society for Testing Materials, Philadelphia, PA., 1976): 306-319.

33. H. Fuhring and T. Seeger, “Structural Memory of Cracked Components under Irregular Loading,” *ASTM STP 677* (American Society for Testing Materials, Philadelphia, PA., 1979): 144-167.

34. A. U. de Koning and G. Liefing, “Analysis of Crack Opening Behavior by Application of a Discretized Strip Yield Model,” *ASTM STP 982* (American Society for Testing Materials, Philadelphia, PA., 1988): 437-458.

35. R. J. H. Wanhill, "Flight Simulation Fatigue Crack Propagation Evaluation of Candidate Lower Wing Skin Materials with Particular Consideration of Spectrum Truncation," NLR TR 77092 U, 1977.

36. R. J. H. Wanhill, "Flight Simulation Fatigue Crack Growth Testing of Aluminum Alloys," *International Journal* of *Fatigue,* 16 (1994): 99-110.

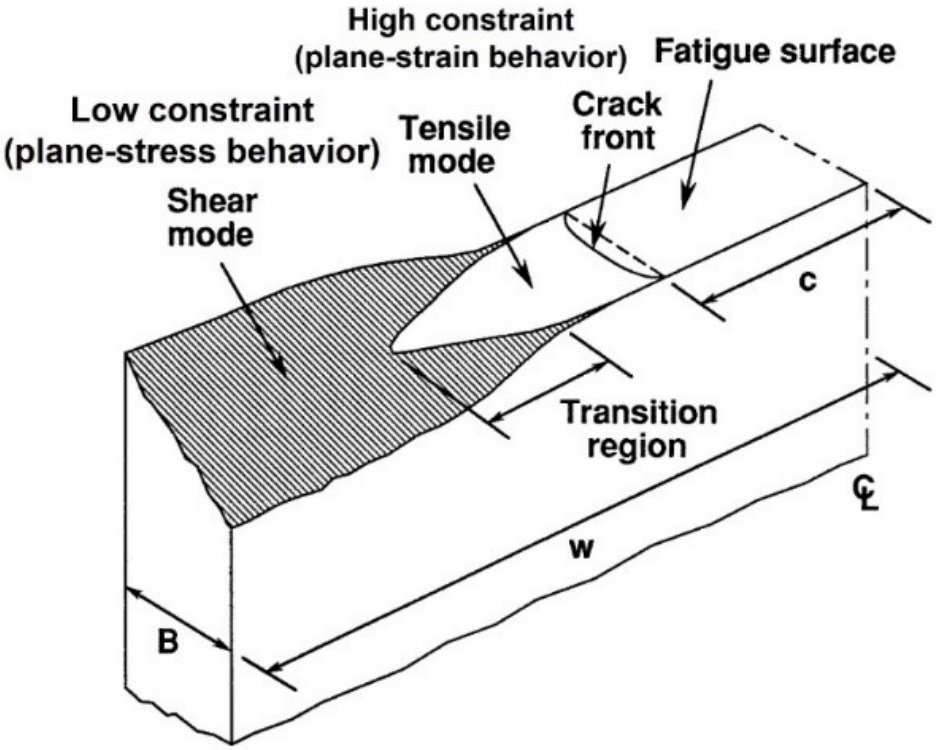

FIGURE 1 Schematic of flat-to-slant fatigue-crack growth in metallic materials.

72x55mm (220 x 220 DPI)

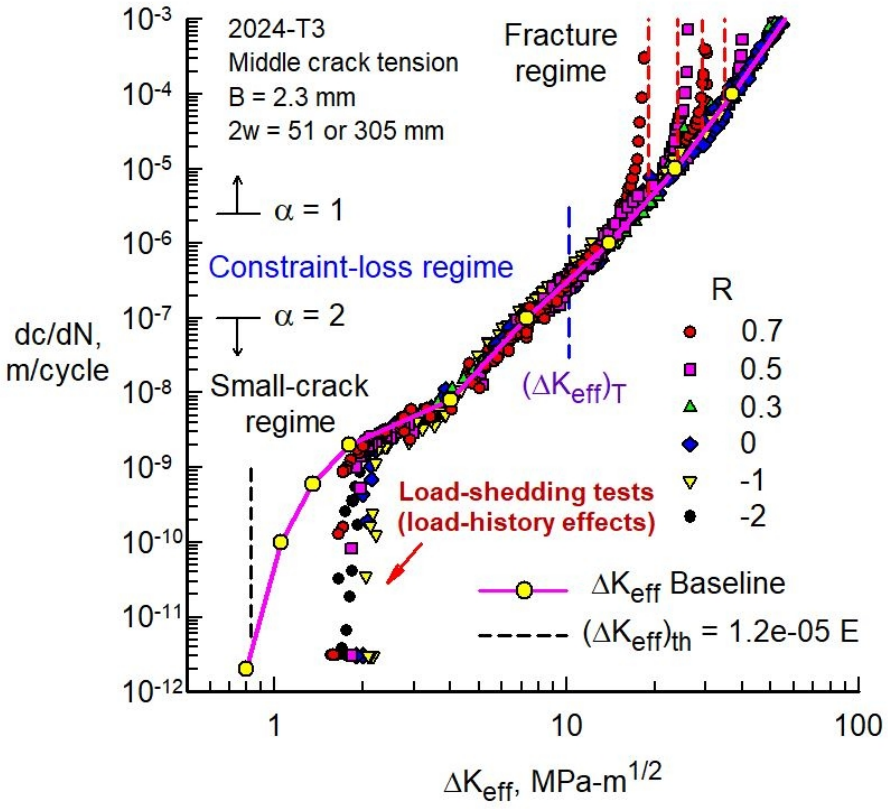

FIGURE 2 Effective stress-intensity factor range against rate for 2024-T3 bare M(T) specimens.

189x162mm (120 x 120 DPI)

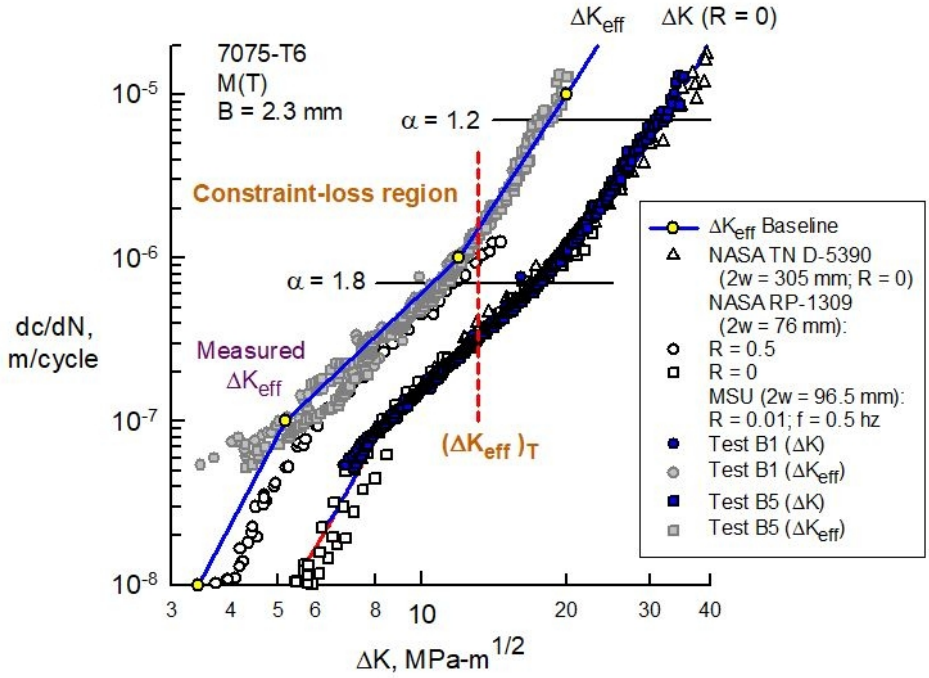

FIGURE 3 Stress-intensity-factor range against rate for 7075-T6 bare M(T) specimens.

164x121mm (120 x 120 DPI)

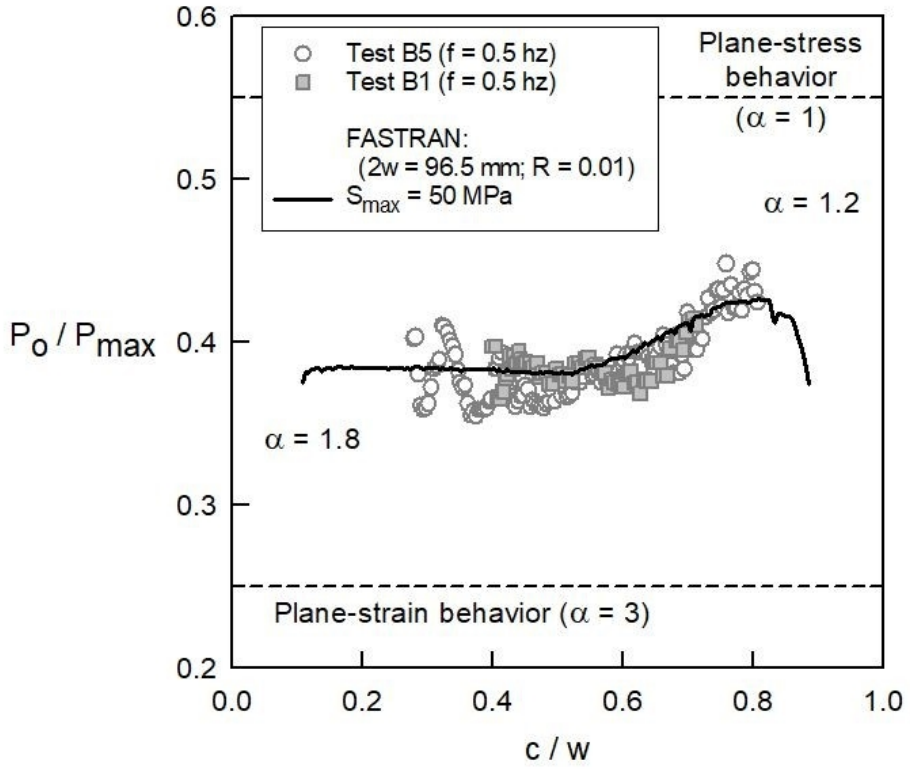

FIGURE 4 Crack-opening-load ratio as a function of crack-length-to-width ratio for 7075-T6 sheet M(T) specimens.

155x135mm (120 x 120 DPI)

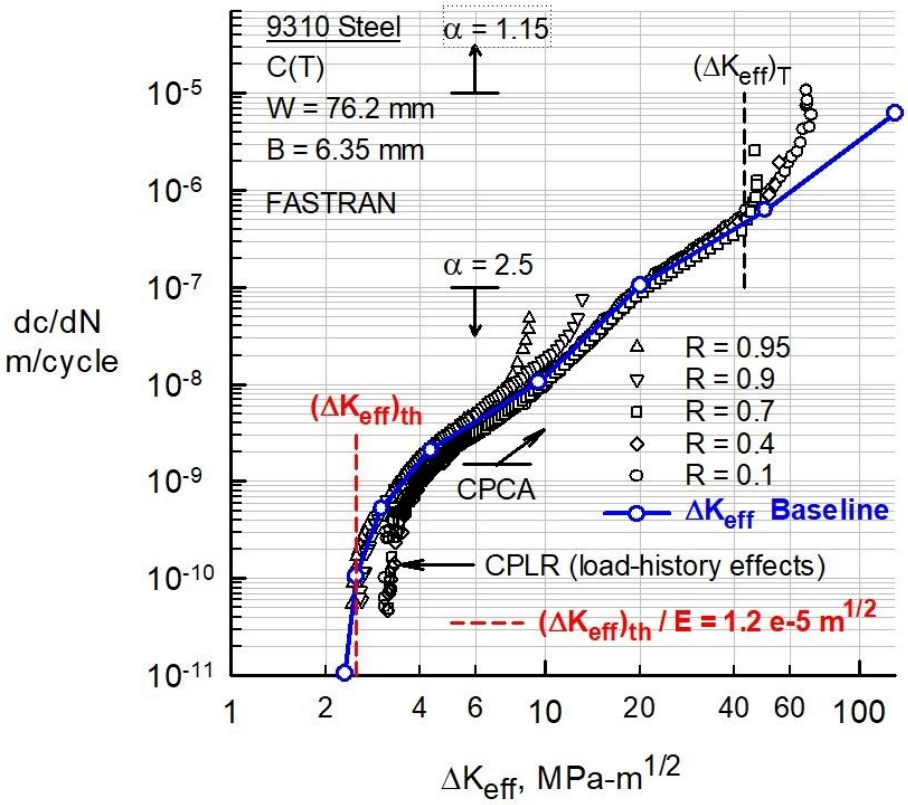

FIGURE 5 Effective stress-intensity factor range against rate for 9310 steel C(T) specimens.

189x161mm (120 x 120 DPI)

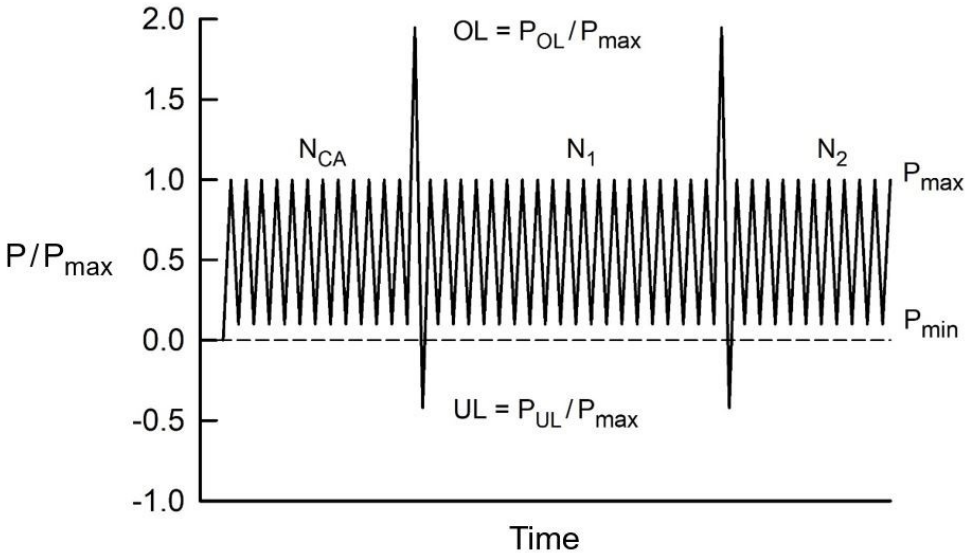

FIGURE 6 Single-spike overload/underload sequence under constant-amplitude loading.

199x131mm (120 x 120 DPI)

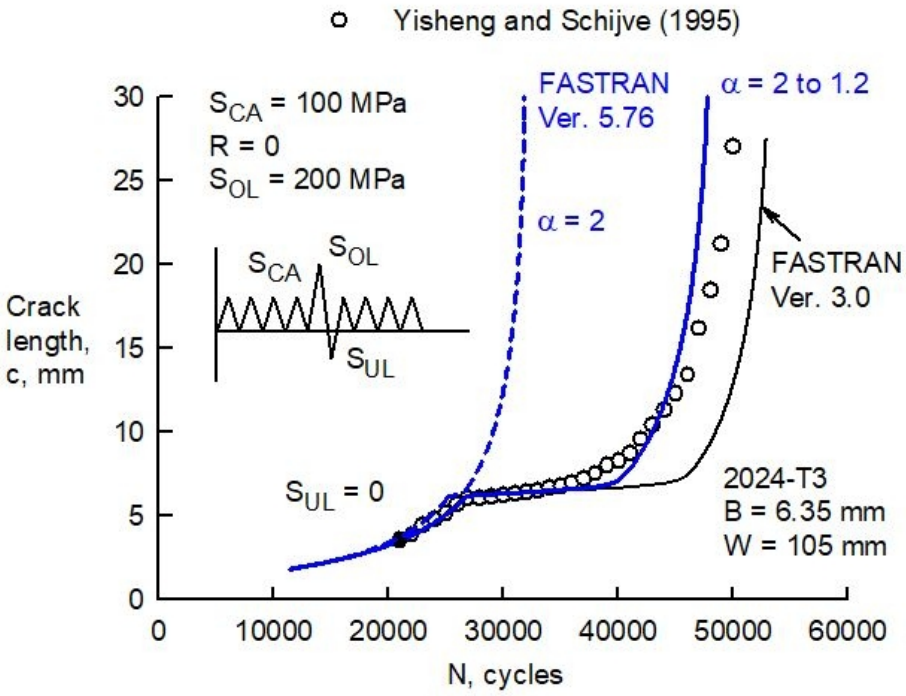

FIGURE 7 Measured and predicted crack-length-against-cycles under a single-spike overload.

141x106mm (120 x 120 DPI)

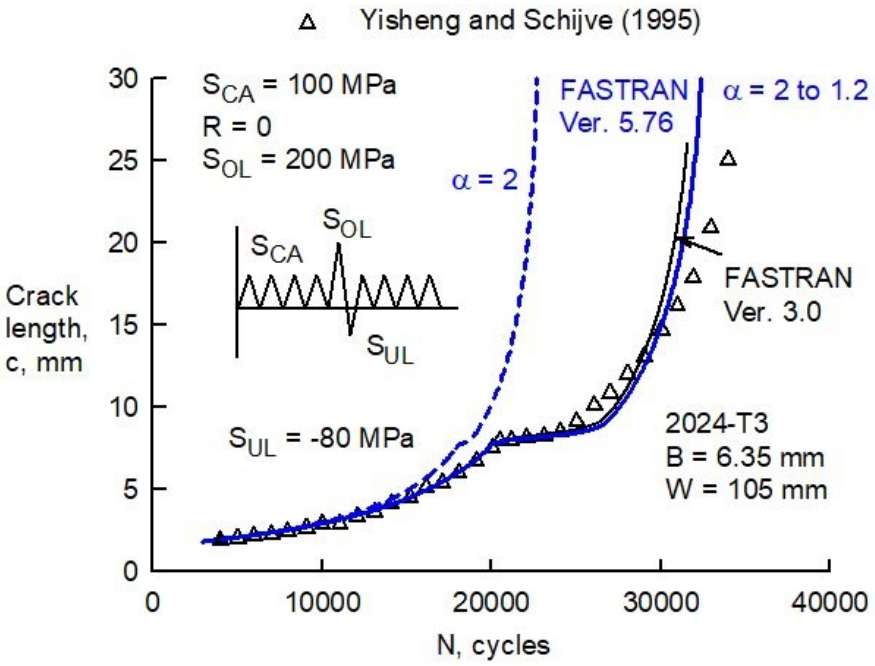

FIGURE 8 Measured and predicted crack-length-against-cycles under a single-spike overload followed by an underload.

144x106mm (120 x 120 DPI)

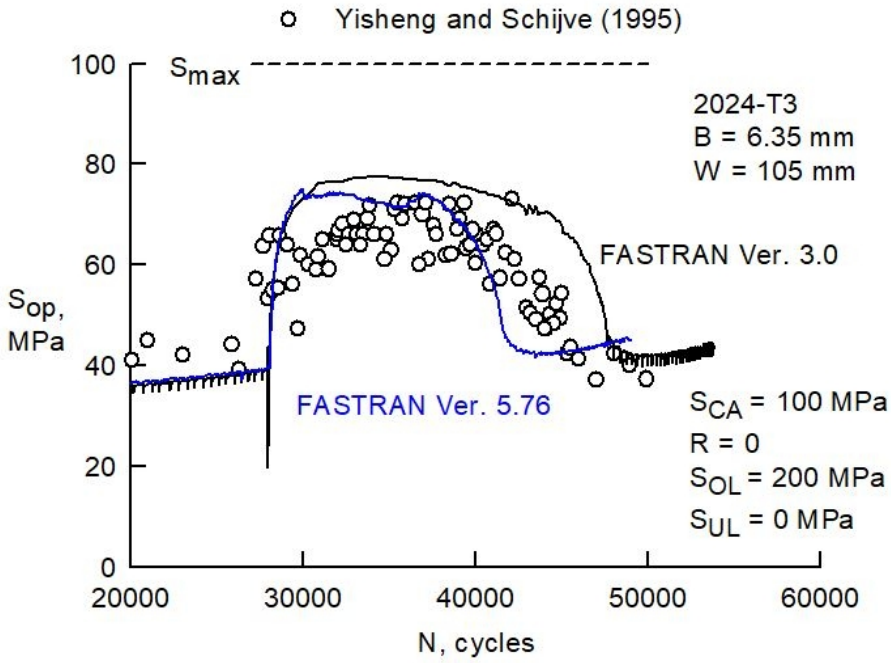

FIGURE 9 Measured and predicted crack-opening stress under a single-spike overload.

161x118mm (120 x 120 DPI)

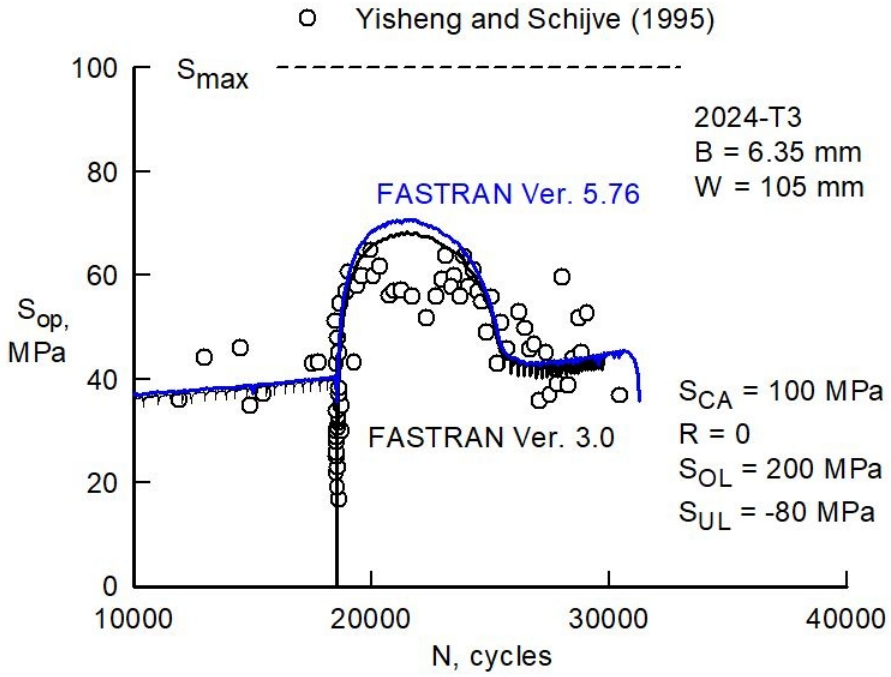

FIGURE 10 Measured and predicted crack-opening stress under a single-spike overload followed by an underload.

176x125mm (120 x 120 DPI)

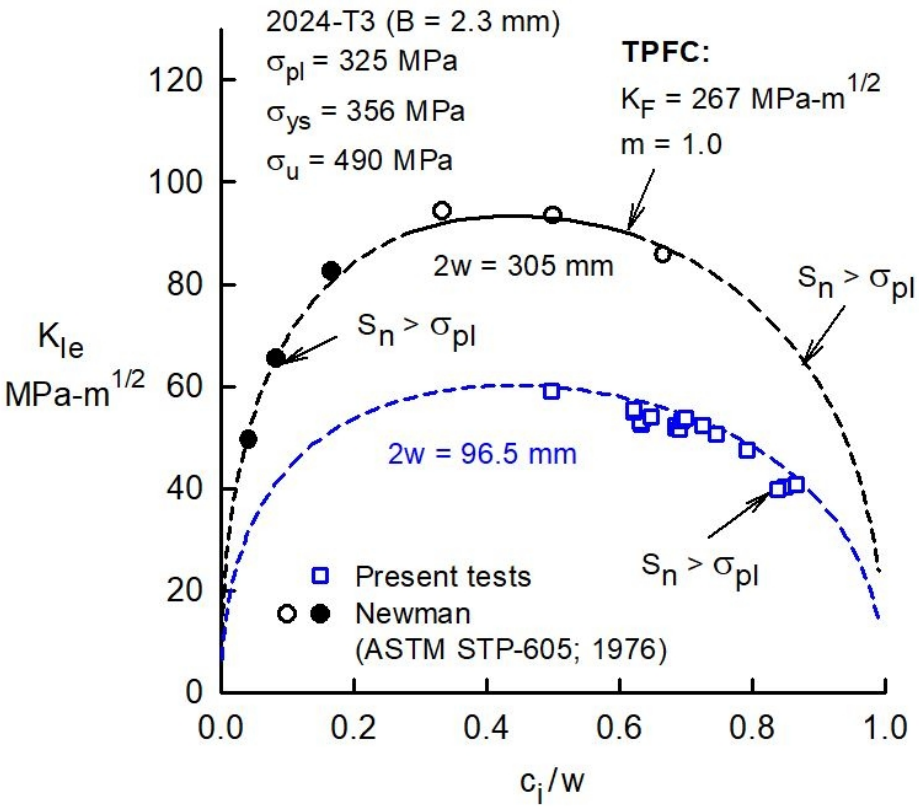

FIGURE 11 Measured and calculated elastic fracture toughness for 2024-T3 bare sheet.

172x139mm (120 x 120 DPI)

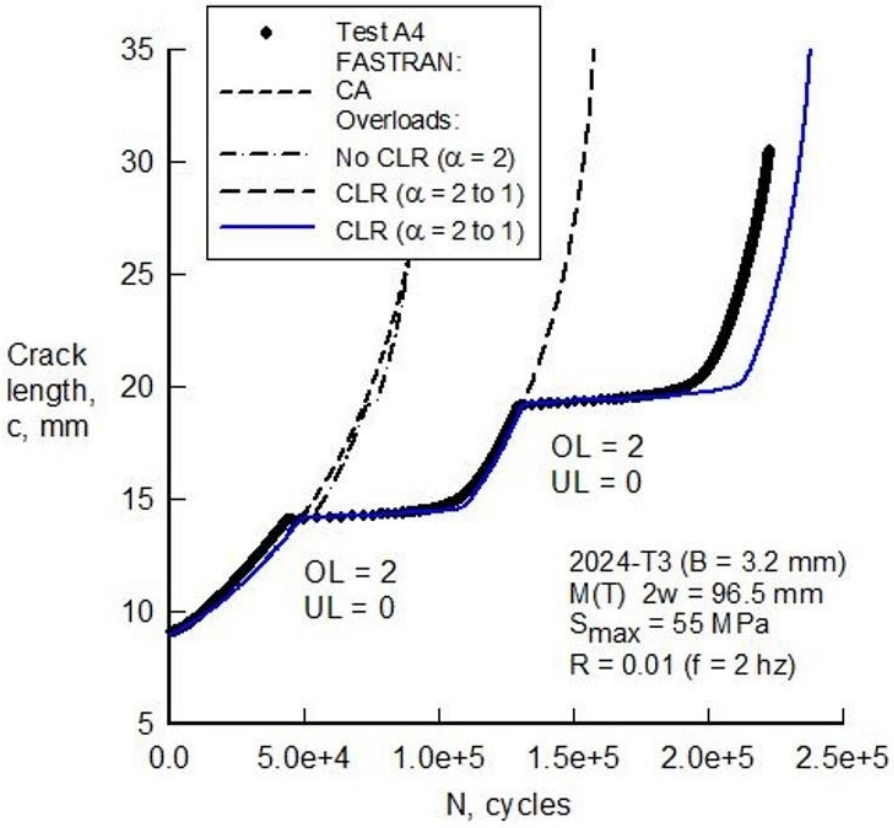

FIGURE 12 Measured and predicted crack-length-against-cycles under single-spike overloads on 2024-T3 bare sheet.

172x144mm (120 x 120 DPI)

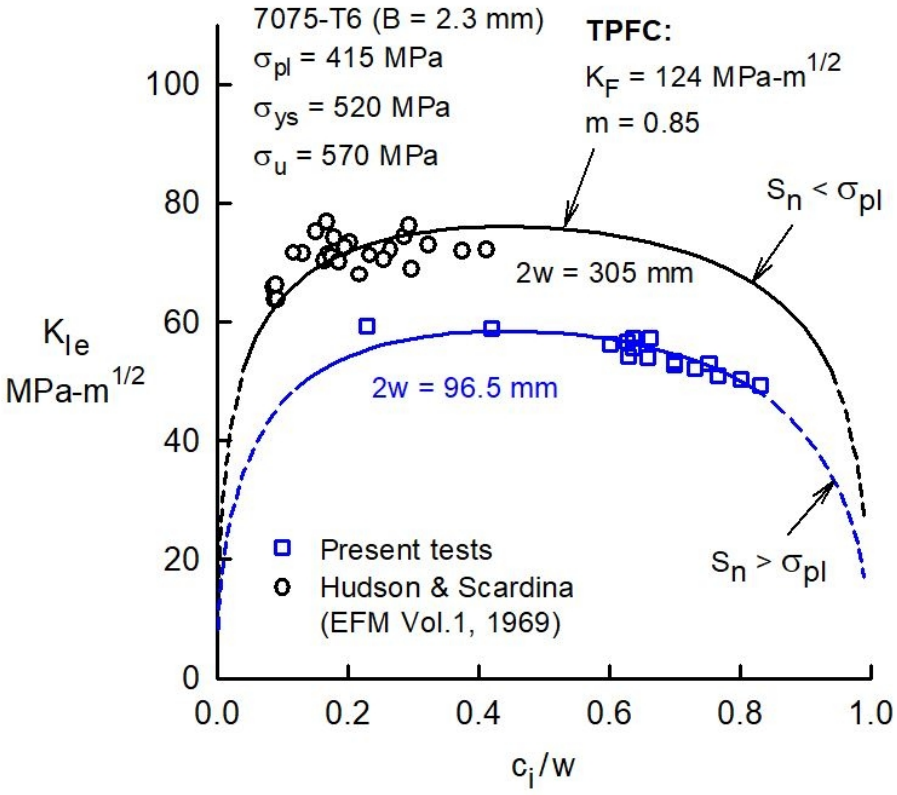

FIGURE 13 Measured and calculated elastic fracture toughness for 7075-T6 bare sheet.

174x147mm (120 x 120 DPI)

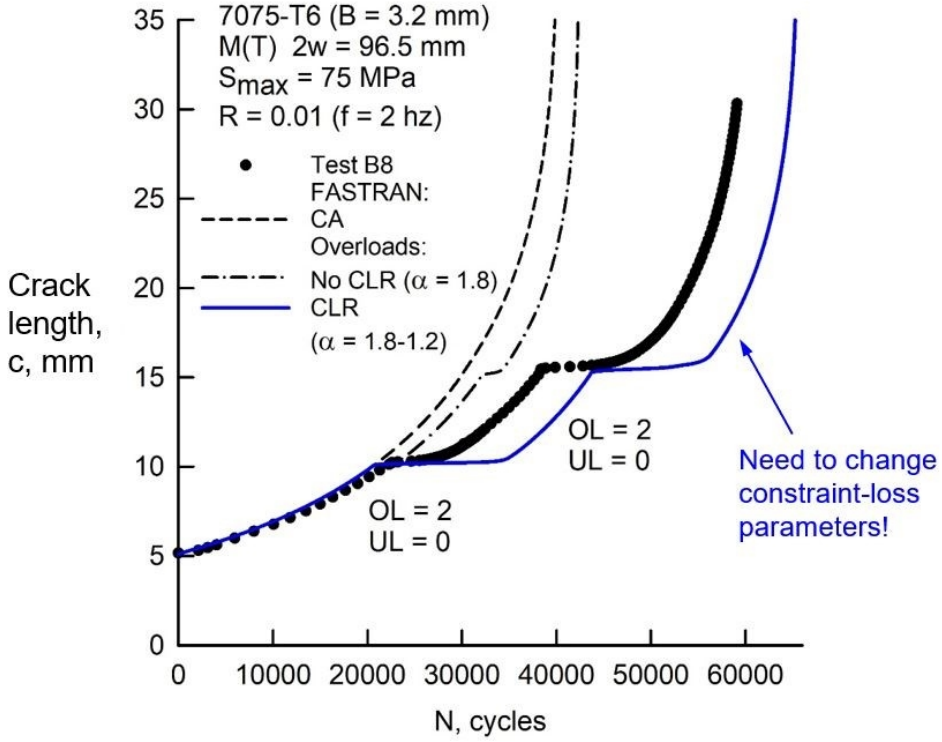

FIGURE 14 Measured and predicted crack-length-against-cycles under single-spike overloads on 7075-T6 bare sheet.

183x140mm (120 x 120 DPI)

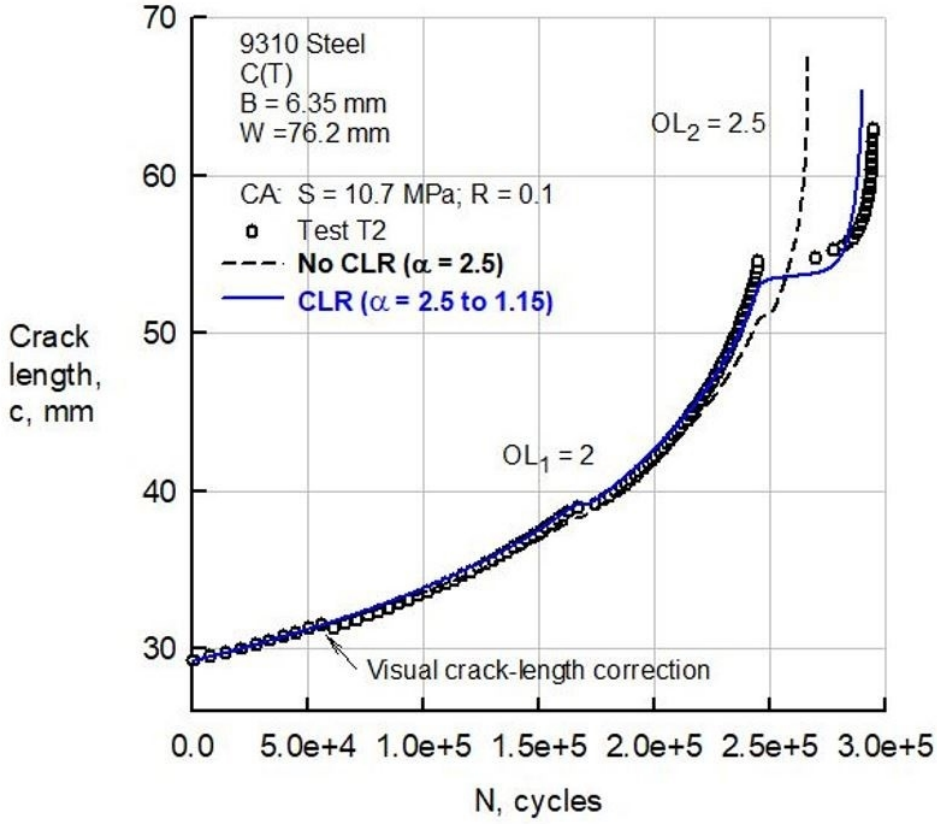

FIGURE 15 Measured and predicted crack-length-against-cycles under single-spike overloads on 9310 steel.

175x147mm (120 x 120 DPI)

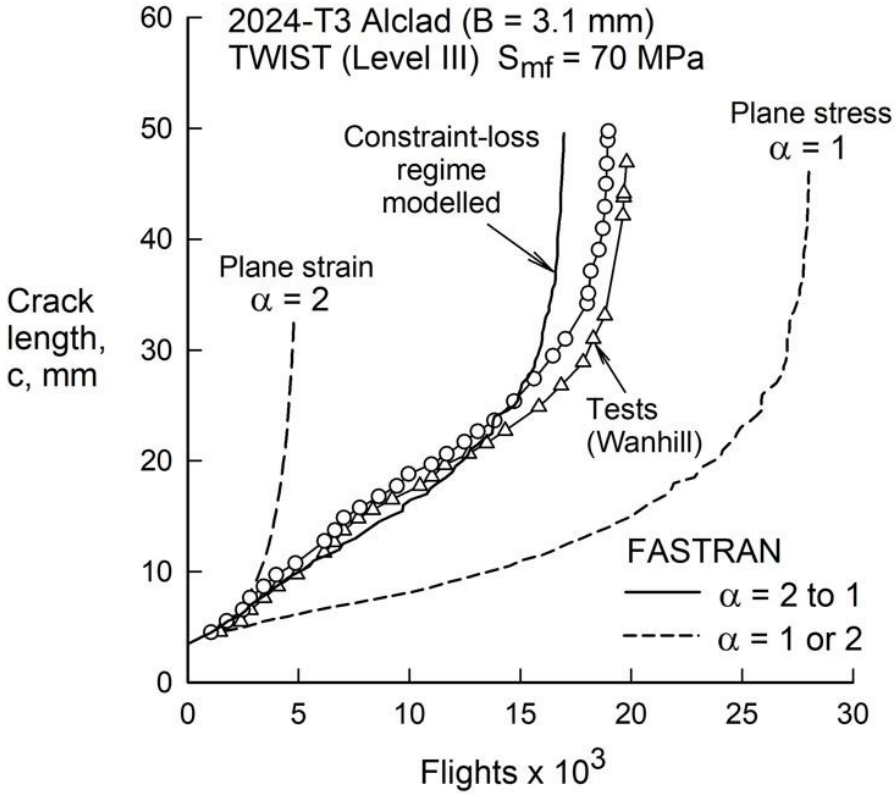

FIGURE 16 Measured and predicted crack-length-against-cycles under TWIST spectrum loading.

173x143mm (120 x 120 DPI)